Dynamics and Composition Measurements in the Lower and Middle Atmosphere with the Purple Crow Lidar

R. J. Sica, P. S. Argall, A. T. Russell, C. R. Bryant* and M. M. Mwangi**
Department of Physics and Astronomy, The University of Western Ontario, London, Ontario, Canada N6A 3K7
sica@physics.uwo.ca

*Now at Department of Physics and Astronomy, University of Calgary, Alberta, Canada
**Now at Department of Physics, Cornell University, Ithaca, NY, U.S.A.

ABSTRACT

The Purple Crow Lidar (PCL) is a large power-aperture product monostatic laser radar which has been in operation at the Delaware Observatory ($42°52′$ N, $81°23′$ W, 225 m elevation above sea level) near the campus of The University of Western Ontario since 1992. The PCL is capable of making simultaneous measurements of Rayleigh, Raman and resonance fluorescence scattering, which allows temperature, constituent density and gravity wave parameters to be simultaneously determined from the troposphere to the lower thermosphere. Temperature measurements are of sufficient accuracy to identify layers of stability and instability in the middle atmosphere. Density fluctuation measurements throughout the lower and middle atmosphere can be used to estimate the spectrum of atmospheric gravity waves at high spatial-temporal resolution. We have used these measurements to isolate individual waves in the vertical wavenumber spectrum, to determine eddy diffusion profiles and to measure the temporal spectrum in the stratosphere past the local buoyancy frequency. We have also begun composition measurements, including the first routine mid-latitude ground-based measurements of water vapour mixing ratio from near the surface to the lower stratosphere. We have also developed and applied a new technique to allow N_2 and O_2 density profiles to be estimated from PCL measurements in the upper mesosphere and lower thermosphere.

I. INTRODUCTION

The fundamental meteorological quantities of temperature, density, wind and humidity are well known near the surface and reasonably well known in the troposphere. However, weather variables in the middle atmosphere, e.g. the region above the troposphere to the turbopause (10 to 115 km) are much more poorly understood. It is clear, however, that general circulation models in the lower atmosphere show significant improvement when they are extended into the middle atmosphere. Hence, it is important to make measurements which can be used to test the reality of general circulation models.

PCL measurements which have improved our understanding of the middle atmosphere are described in this review. First, a description of the system configuration and hardware is given, followed by an overview of our temperature measurements. The mesospheric inversion layers are then discussed in some detail, followed by a summary of our results concerning gravity waves and superadiabatic layering. Composition measurements are discussed in the final two sections. We describe our measurements of troposphere and lower stratospheric water vapour and then introduce a new technique which allows the determination of N_2 and O_2 altitude profiles from concurrent Rayleigh-scatter lidar backscatter measurements and an independent temperature determination such as those obtained from sodium resonance fluorescence scattering measurements.

Current information about the PCL, including color versions of many of the following figures, is available at our web site (http://pcl.physics.uwo.ca).

II. PCL SYSTEM DESCRIPTION

The hardware for an atmospheric lidar system can be conveniently divided into two components, the transmitter and the receiver. The transmitter of a lidar generally consists of a pulsed laser system with beam expanding optics and steering mirrors that are used to direct the light into the sky. Once in the atmosphere the laser light interacts with the constituents of the atmosphere and a portion of the emitted laser photons are scattered back to the lidar receiving system. By utilizing a variety of laser wavelengths, atmospheric scattering processes and detection techniques, a number of atmospheric parameters can be measured using the lidar technique. The transmitter and receiver systems for the PCL are described below.

II.1. PCL Transmitter

The type of laser system employed in a lidar depends in large part on the quantity the lidar has been designed to measure. Rayleigh and Raman-scatter lidars utilize the forms of scattering implied by their respective names. Both these forms of scattering occur over a wide range of wavelengths and so do not require a particular laser wavelength. The choice of the type of laser to be used in a Rayleigh-Raman lidar needs to take into account many factors including the backscatter cross section at the laser wavelength, the atmospheric transmission at the laser wavelength, the ease of use and affordability of the laser and the efficiency of detectors at the detection wavelength.

The laser used in the transmitter for the Rayleigh and Raman channels of the PCL to optimize the above trade-offs is a frequency doubled Nd:YAG. The basic parameters of the PCL Rayleigh and Raman transmitter is summarized in Table 1. The output of this laser is expanded in order to reduce the divergence of the beam and transmitted vertically into the sky coaxially with the receiving telescope. Reducing the divergence of the transmitted laser beam allows the field-of-view of the detection system to be reduced, which lowers the number of multiply scattered photons, scattered moon light, star light and anthropogenic sources which are detected as a background.

Transmitting the laser beam along the axis of the detection telescope significantly reduces the possibility of an overlap error in the alignment of the laser beam and the field-of-view of the detection system. If the fraction of the laser beam that is within the field-of-view of

Table 1. Specifications of the PCL Rayleigh and Raman transmitter.

Wavelength	532 nm
Energy per pulse	600 mJ
Repetition rate	20 Hz
Pulse length	7 ns FWHM
Beam diameter	27 mm
Beam divergence at e^{-2}	0.2 mrad, full width

the detection system changes with altitude an error would result in the temperatures derived from the Rayleigh lidar.

The transmitter for the sodium-resonance-fluorescence system (henceforth the Na system) is much more complex than that of the Rayleigh-Raman transmitter. The Na lidar temperature measurements require measurements of the spectral width of the Na D_{2a} line. This measured line width is then used to determine the temperature of the mesopause region of the atmosphere.
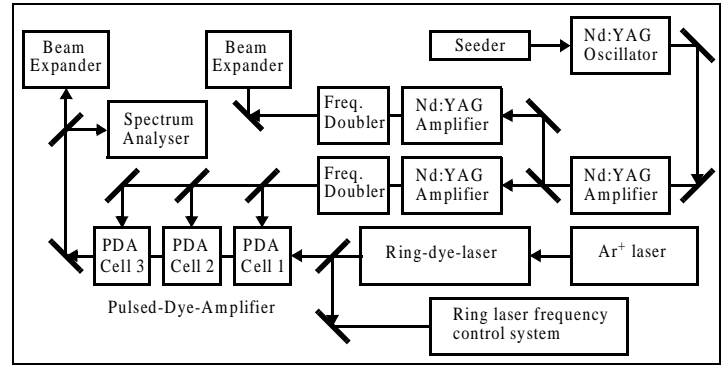

Figure 1. Schematic of the PCL transmitter system.

In order to measure the Na D_{2a} line's spectral width the PCL uses a narrow line width laser that can be tuned across the Na D_{2a} line. A combination of several lasers is required to produce the pulsed, tunable, narrow-band and relatively high power light source required for the Na lidar temperature measurements (Figure 1). The Na transmitter comprises a tunable narrow-band (500 kHz) ring-dye-laser (RDL) which is pumped by an Ar^+ laser operating at 4 W. The cw beam from the RDL is used to seed a 3 stage pulsed-dye-amplifier (PDA) which is pumped by a 600 mJ per pulse, 20 Hz frequency doubled Nd:YAG beam. The PDA output is 6 0mJ per pulse at 20 Hz with a spectral width of about 106 kHz. This beam is expanded to a diameter of 2 7mm and transmitted into the sky coaxially with the detector system field-of-view.

A sample of the output of the RDL is directed into the ring-laser-frequency-control-system (RLFCS; Figure 1). The RLFCS uses a technique known as Doppler-free-saturation-spectroscopy (DFSS) to actively lock the

RDL's output frequency to a frequency marker that is generated by a cell containing Na vapour. The frequency markers that are generated using this technique lie within the Na D_{2a} line. Further details of the narrow-band Na technique and the use of DFSS are found in Argall et al. (1) and the references therein.

II.2. PCL Receiver

The receiving system for the PCL is based on a 2.65 m diameter liquid mirror telescope (LMT), which is described by Sica et al. (2). Light backscattered from the atmosphere is focused by the LMT onto the plane of the entrance aperture of the detection system shown in Figure 2. Light that is reflected from the LMT then passes through the entrance aperture of the detection system and is collimated by lens L1. The dichroic-beam-splitter, DBS1, reflects the two Raman wavelengths of interest for water vapour measurements onto DBS2 which reflects the nitrogen Raman wavelength (607 nm) and transmits the water vapour Raman wavelength (660 nm). Light at these two wavelengths is then incident on 1.0 nm bandwidth interference filters, centered at the appropriate wavelengths. The light transmitted by the interference filters is focused onto photomultiplier tubes.
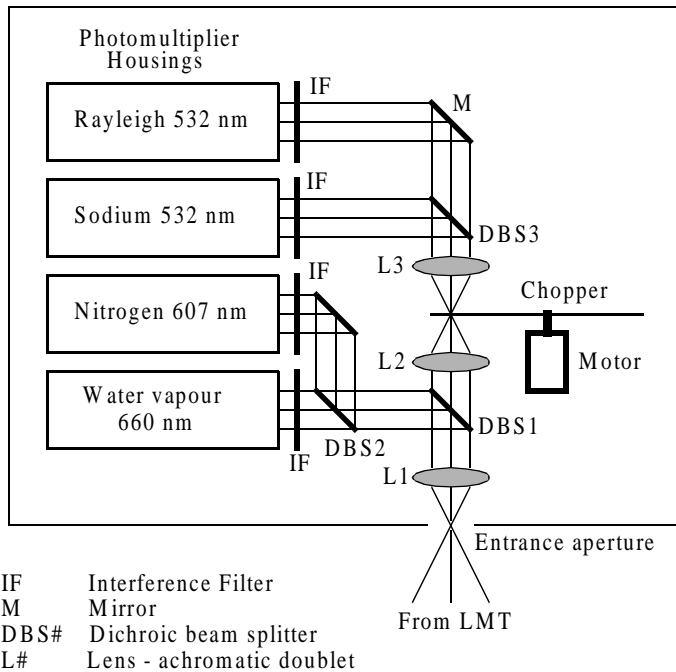

Figure 2. Schematic of the PCL detector system.

Light at the Rayleigh (532 nm) and Na (589 nm) wavelengths is transmitted by DBS1 to a rotating chopper which removes low altitude (below 25 km) returns. Light transmitted by the chopper is split by DBS3 into Rayleigh and Na beams. These two beams pass through 1.0 nm interference filters and onto photomultiplier

tubes. All four photomultipliers used in this detection system are Hamamatsu model R5600P-01 miniature photomultipliers.

The PCL Raman system ratios the Raman backscatter from water vapour and molecular nitrogen to achieve a measurement of the water vapour mixing ratio. It is therefore important that the ratio of the optical efficiency of these two channels does not change with altitude. Careful optical design of the receiver system ensures that this ratio is constant with altitude.

The optics of the PCL detector system have been designed so that the LMT forms the limiting pupil of the system and the entrance aperture of the detector housing forms the limiting aperture (Figure 2). This choice of limiting pupil guarantees that no vignetting occurs inside the detector housing. Thus, each of the detection channels sees exactly the same field-of-view through exactly the same pupil.

The two Raman channel photomultipliers are connected via 300 MHz discriminators (Phillips Scientific, 6904) to PC-card type multichannel scalars (Nucleus). The Rayleigh and Na channel photomultipliers are connected to Stanford Research multichannel scalars (SR 430) which have a maximum count rate of 100 MHz.

Due to the high power-aperture product of the PCL significant nonlinearities in the counting of the photomultiplier pulses occurs for three of the four detection channels. The Raman water vapour channel does not suffer from this problem because of the low signal levels in this channel.

Using a light-emitting-diode (LED) and signal generator an optical signal resembling the intensity distribution of the actual lidar returns can be simulated. These simulated returns, measured with and without an optical attenuator, allow a correction for the counting system nonlinearities to be determined. This correction is applied to the atmospheric backscatter measurements as part of the data reduction.

III. Temperature Results

III.1. Rayleigh Temperature

The Rayleigh lidar technique is a well established method for providing high resolution temperature measurement from the middle of the stratosphere up to the lower thermosphere (2,3).

A Rayleigh lidar measures the number of backscattered laser photons as a function of altitude, i.e.

$$N(z) = C \frac{n(z)}{z^2} , \qquad (1)$$

where N is the number of photons detected, z is the altitude, n is the atmospheric number density and C is a constant that includes the effects of parameters such as laser power, detector system efficiency and collecting area, transmission of the lower atmosphere and the Rayleigh backscatter cross section of air.

The calibration constant, C, in Equation 1 cannot be determined precisely due to uncertainties in instrumental parameters and the transmission of the lower atmosphere. Thus, $N(z)$ is a relative density profile. This relative density profile can be scaled using a model atmosphere, over an extended altitude range, so it is reasonably well scaled. However, temperature determinations only require a relative density profile.

Temperature is found from the relative density using the Ideal Gas Law and assuming that the atmosphere is in hydrostatic equilibrium, i.e. the pressure at any altitude is equal to the weight of the air above that level. Chanin et. al. (3) and Shibata et. al. (4) describe the details of calculating an absolute temperature profile from a relative density profile. Using this method to determine an absolute temperature profile requires an estimate of the actual temperature or pressure at the uppermost altitude at which measurements are available. This estimate is required to seed the temperature retrieval integration algorithm. Of course, this uncertainty can be eliminated if the temperature is known. The coincident PCL Na temperature lidar measurements offer the possibility of making absolute temperature measurements in this region, which could then be used to seed the Rayleigh temperature retrieval algorithm. Argall et al. have shown some initial results of such temperature seeding (1).

An error in the initial temperature (pressure) will manifest itself as an error in the calculated absolute temperature profile. Generally, absolute temperature measurements made coincidently with Rayleigh measurements at 100 to 110 km are generally not available and model atmospheres are used to initiate the temperature retrieval algorithm. The magnitude of the initialization error in the temperature retrieval reduces quickly as the integration progress downward in altitude. An error of 10 K in the estimate of the initial temperature is reduces to less than 3 K at 10 km below the initialization altitude. All of the temperatures presented here have been calculated from temperature profiles that have had the top 10 km removed. This procedure ensures that the measurements presented are not significantly influenced by this initialization effect.

The Rayleigh lidar temperature measurement technique works in the altitude range of approximately 25 to 100 km. Below 25 km scattering from the stratospheric aerosol layer contaminates the measured Rayleigh signal and cannot be removed without very precise spectral measurements of the backscattered light. A correction for the optical transmission of the atmosphere due to ozone in the altitude range of 25 to 50 km is also necessary for the temperature retrievals. Corrections for this effect are given by Sica et. al. (5). The application of this correction leads to a temperature difference of about 0.5 K at 30 km and is wavelength dependent.

The upper altitude limit for the Rayleigh temperature technique is generally considered to be about 100 to 110 km. This altitude limit is based both upon the composition changes that occur above these altitudes, as well as the signal-to-noise ratio limitations of current Rayleigh lidars. The uncertainties introduced into Rayleigh lidar temperature measurements because of composition changes in the lower thermosphere are not addressed in the current analysis scheme, but should be considered in the future (see Section VII).
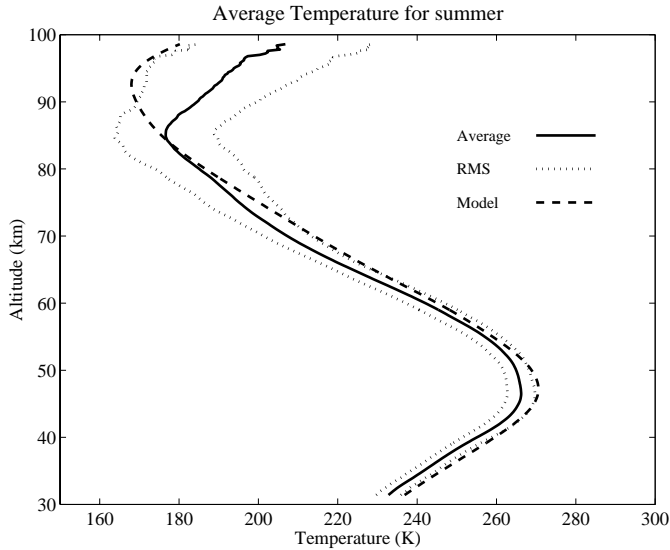
Changes in atmospheric composition leads to changes in both the Rayleigh backscatter cross section and the mean molecular mass of air. Changes in these two parameters must to be taken into account in the Rayleigh temperature retrievals at higher altitudes. Generally this composition information is not available and so this type of correction may not be possible. Section VI discusses how the Rayleigh scatter measurements, combined with Na lidar temperature measurements, can be used to determine composition information in the altitude range 85 to 105km.

The PCL has been routinely measuring Rayleigh temperatures since early 1994 and continues to operate on most clear nights. The majority of the PCL measurement are between mid spring and mid fall, corresponding to the time of year when the probability of clear sky is greatest. Table 2 shows the distribution of the PCL Rayleigh lidar temperature set. The bias toward the summer months is obvious.
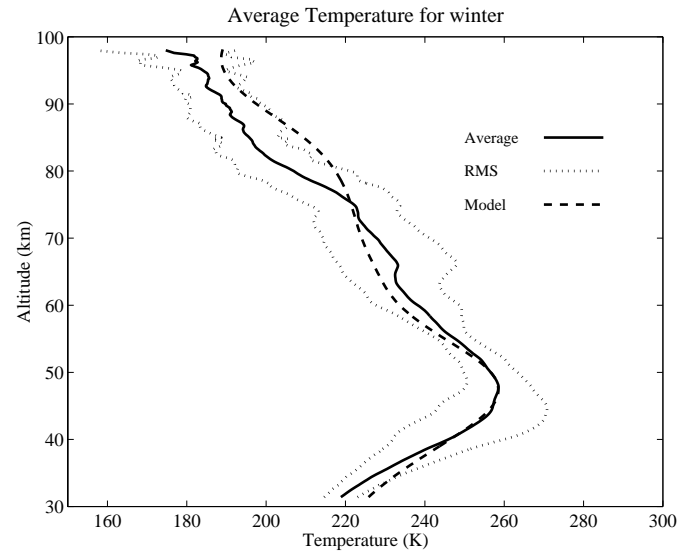
Figures 3 and 4 show summer (June, July, August) and winter (December, January, February) average temperature profiles calculated from the PCL Rayleigh measurements. The average for the summer months is significantly lower than predicted by the model of Fleming et. al. (6) from 31.5 km to 74km. In fact, the sum of the mean lidar temperature and the RMS deviation from the mean is very similar to the temperature of the model over the entire range of 30 to 70km. However, the most striking feature is the altitude of the mesopause, which is observed at 85 km. This height is about 7. 5km lower than suggested by the Fleming et al. model. This lower summer mesopause is in agreement with measurements obtained by Na lidar systems (e.g. Senft et. al. (7)). The

Table 2. Rayleigh temperature measurements by month.

Month	# of nights
January	2
February	9
March	7
April	15
May	31
June	41
July	46
August	62
September	32
October	31
November	18
December	10
Total	**304**

Figure 4. Average temperature for winter calculated from 21 nights of PCL Rayleigh lidar measurements taken from 1995 to 2000.

Figure 3. Average temperature for summer calculated from 149 nights of PCL Rayleigh lidar measurements taken from 1994 to 1999.

RMS values in Figure 3 and 4 represent the RMS deviation of the individual nightly averaged temperature profiles from their respective means. There is a contribution to this RMS value from two sources. The dominant source is the geophysical variations in the temperature. Statistical uncertainties in the nightly averaged temperatures also contribute to the RMS. The average of the statistical uncertainties for the nightly averaged temperature profiles used in calculating the summer average is 1 K to 70 km, then increasing to about 5 K at 98 km. The average PCL temperature profile for winter (Figure 4) illustrates the more dynamic state of the atmosphere in these months. The average profile is not as smooth as the summer average for two reasons. First, only 21 nights of measurements are used in this average while 149 nights are used in the summer average. Sec-

ond, the variations between individual nights below 75 km is much greater in the winter, as can be seen in the larger RMS deviations at these altitudes. The combination of these two effects leads to the summer average being smoother than the winter average.

The winter average is cooler than the model at 31.5 km by about 7 K but the temperature increases rapidly so that the stratopause altitude and temperature are consistent with the model. The PCL measurement above 80 km are again several degrees colder than the model and do not show a mesopause in the winter average.

The RMS deviations from the mean for the winter show more structure than those for the summer. There is a maximum in the winter RMS just below the stratopause, where the RMS is 16 K. The RMS deviations then decrease to about 5 K at 55 km. The RMS deviations then increase sharply to 15 K again at 68 km. Above 85 km the effects of statistical fluctuations in the nightly averages are a significant fraction of the RMS values. This means that the geophysical variations in temperature above 85 km are less than is indicated by the RMS values, so that the region between 90 and 97 km is actually less variable in winter than in the summer.

Temperature variability due to mesospheric inversions (discussed in detail in the next section) cause the rapid increase in the RMS deviation in the 55 to 68 km altitude range. The minimum in the RMS is at 55 km, an altitude below which the inversions do not propagate. The increase in the RMS at 42 km is not the result of a downward propagation of the mesospheric inversion into the stratosphere, although it may in fact be related to the inversion in the mesosphere.

III.2. Sodium temperatures

The Na lidar technique uses a measurement of the spectral shape of the resonantly scattered light from neutral Na atoms to determine the atmospheric temperature. A layer of Na atoms exists in the atmosphere between about 85 and 105 km due to the deposition of Na, as well as other metallic species, from the ablation of meteors at these altitudes.

Na lidar uses a laser that is tuned to the Na D_{2a} line. Resonant scattering at this frequency is many orders of magnitude greater than that for Rayleigh scatter at the same wavelength. This large cross section allows a reasonable signal-to-noise measurements to be obtained by Na lidar despite the small amount of sodium present.

To achieve a measurement of the spectral shape of the backscattered light from the Na layer the PCL transmits alternately groups of pulses at two precisely defined wavelengths within the Na D_{2a} line. The ratio of the intensity of the backscatter at these two wavelengths is a measure of the line shape and can be directly related to the kinetic temperature. Further discussion of this method and a detailed error analysis of the PCL Na lidar system can be found in Argall et. al. (1).
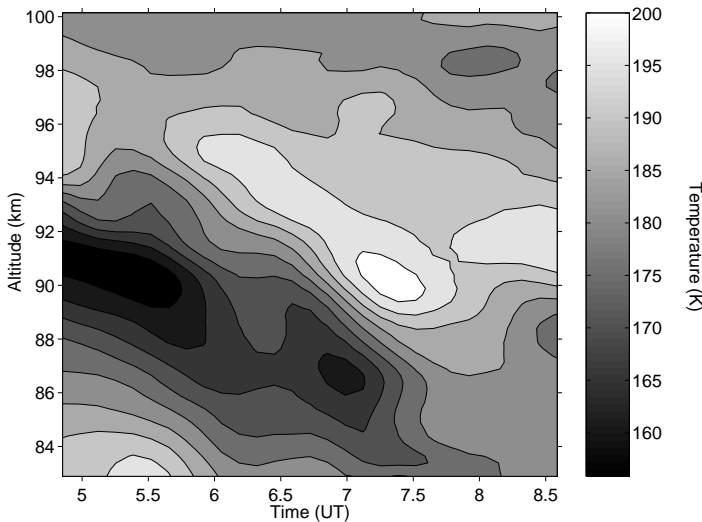

Figure 5. Temperatures measurements at 8 min temporal and 250 m vertical resolution made by the PCL Na resonance fluorescence lidar.

Figure 5 shows the evolution of the temperature profile measured with the PCL Na lidar on the night of May 21, 1998. This figure illustrates the dynamic state of the atmosphere in this region. At an altitude of 91 km the temperature changes from 155 K at 0530 UT to 200 K at 0715 UT, a change of 45 K in less than 2 hours.

Both the Rayleigh and Na lidar techniques provide powerful tools for remotely monitoring atmospheric temperature. Having a lidar able to make both Rayleigh and Na measurement simultaneously extends the useful-

ness of both techniques. Na temperature measurements can be used to seed the Rayleigh temperature retrieval algorithm, improving the derived temperatures. The combination of the measurements also allows some composition information to be obtained. One feature of the atmospheric temperature structure which has been studied in some detail are inversion layers in the mesosphere.

IV. MESOSPHERIC INVERSION LAYERS

It is well known that inversions with temperature increases on the order of tens of degrees routinely occur in the mesosphere and lower thermosphere (8,9). Leblanc and Hauchecorne (10) have studied the seasonal variations of inversions and found that the inversions are stronger in the winter months at midlatitudes, while the inversions measured during the summer months are strongest at lower latitudes. They also found that many inversions have an extended longitudinal structure, as opposed to being a local phenomena.

What is the cause of these inversions? Most explanations of mesospheric inversion layers involve atmospheric waves, though Whiteway et al. (11) have suggested that the inversions form due to turbulent mixing in a manner similar to the formation of the planetary boundary layer. Hauchecorne et al. (9) suggested that the inversions are due to gravity waves breaking within the inversion region for extended periods. Evidence that tides are also involved was presented by Dao et al. (12) and States and Gardner (13). Subsequently, Meriwether et al. (14) have suggested that tidal modulation of gravity wave forcing is the key to the formation of the inversions.

The high temporal-spatial resolution of the Purple Crow Lidar has revealed two new properties associated with mesospheric inversions. The first property is the variability of these structures over time. While many nights show inversions in the nightly average, temperature variations of 5 to 10% in the actual inversion layer are not uncommon. The second property is that these inversions appear to exist in two distinct classes. Lower mesospheric inversions are the inversions typically discussed in the literature. Lower mesospheric inversions persist from night to night (Figure 6). However, in the summer months the inversion occur frequently at altitudes around 75 to 80 km. These higher altitude inversions are variable over a night and appear to be related to the tides.

The role of gravity waves in the inversion layers is not directly evident from the PCL measurements. The lower mesospheric inversion layer shown in Figure 7 at 65 km altitude is associated with kinetic energy densi-
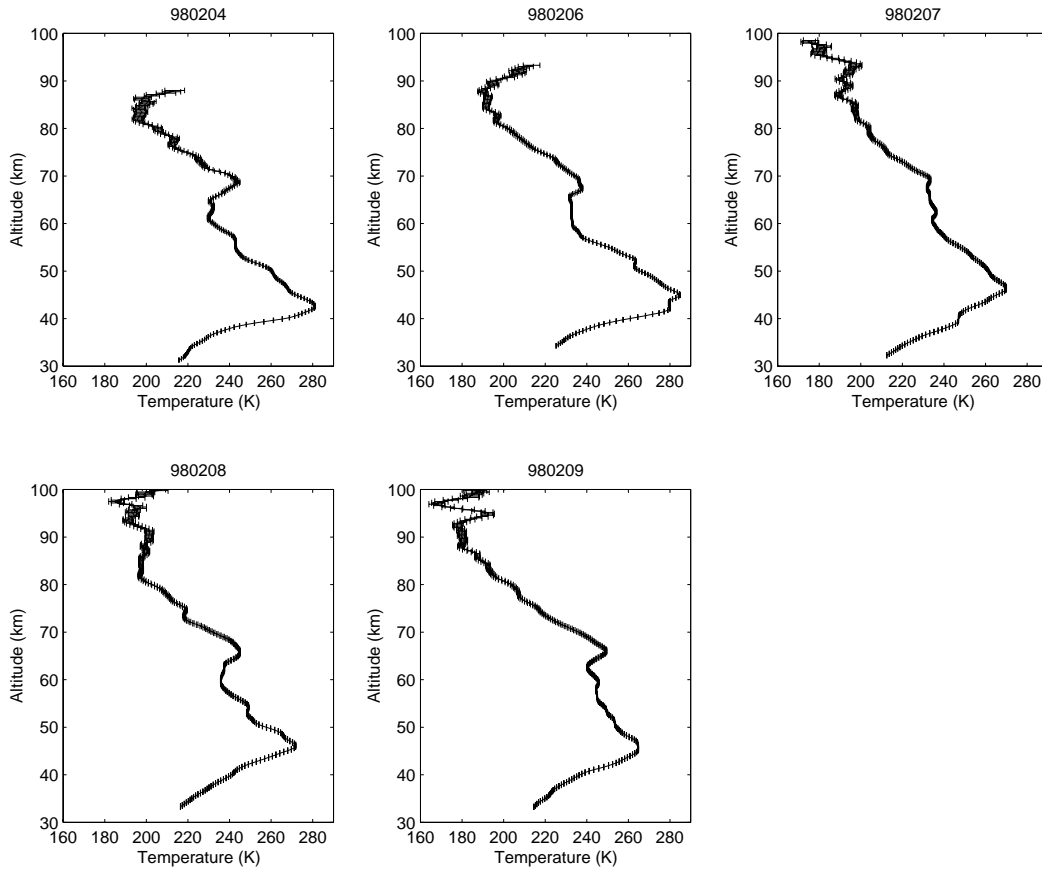
Figure 6. Nightly temperature averages from early February, 1998. The horizontal bars indicate plus and minus one standard deviation of the measurement error.

ties below, in and above the inversion region that are not appreciably different from comparable summer measurements when no inversions exist. The inversion "turns on" between 0000 and 0200, with temperature increases on the order of 20 K, which persist until the end of the measurements at 1045 UT. The total kinetic energy density per unit mass, however, is largest during

the 0000 to 0200 UT period when the inversion is weak, decreasing from 200 $(m/s)^2$ to 50 $(m/s)^2$, then increasing after 0900 UT as the inversion strengthens.

Upper mesospheric inversions are observed more frequently in the summer and exhibit both temporal variability and evidence of tidal modulation (15). Mesospheric temperature profiles for the first and second half of the measurement period on July 31, 1998 show the variability associated with an upper mesospheric inversion (Figure 8). In contrast to the lower mesospheric inversions, the upper mesospheric inversions are weaker, though the kinetic energy densities are similar to the measurements of the lower mesospheric inversions. Figure 9 shows determinations of the upper mesospheric tide from measurements by the UWO MF radar (performed by Drs. T. Thayaparan and W. Hocking, see Thayaparan et al (16)) compared to the temperature changes in the inversion region. The zonal semidiurnal tide was dominant and highly correlated with the temperature change. As the semidiurnal tide decreased in its westward phase, the inversion layer appeared.

On June 1, 1998 the inversion layer occurs in the first half of the evening (Figure 10). The inversion is accompanied by a significantly steeper average mesos-
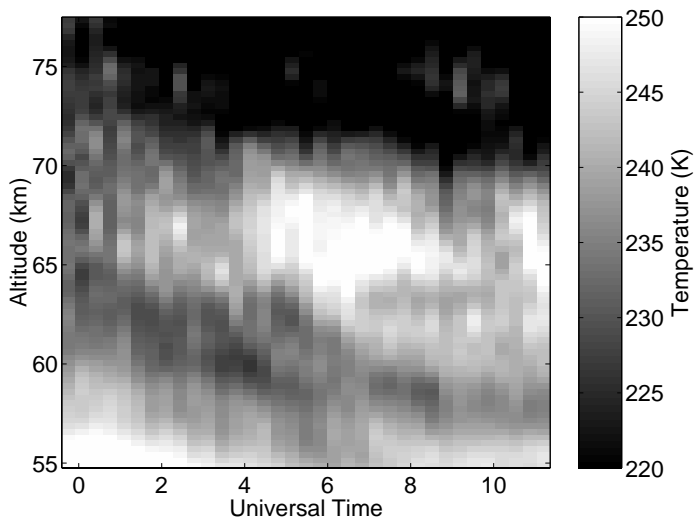

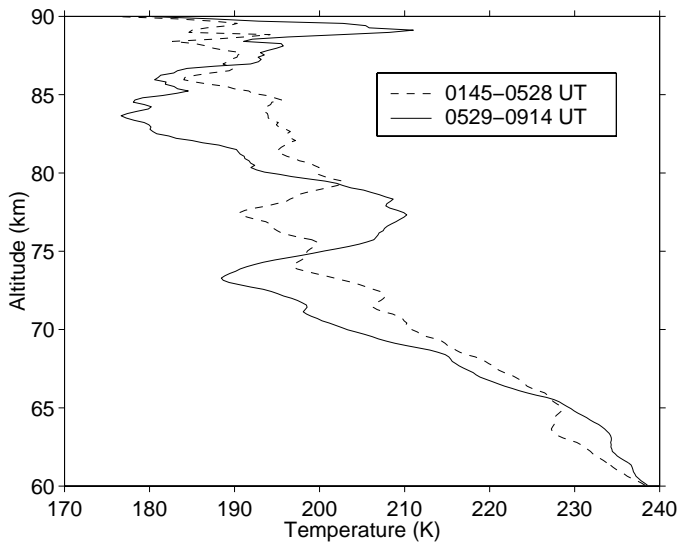**Figure 7.** Increase of the strength of a mesospheric inversion layer on February 8, 1998.

Figure 8. Comparison of mesospheric temperature profiles between the first and second halves of the observing period on July 31, 1998.
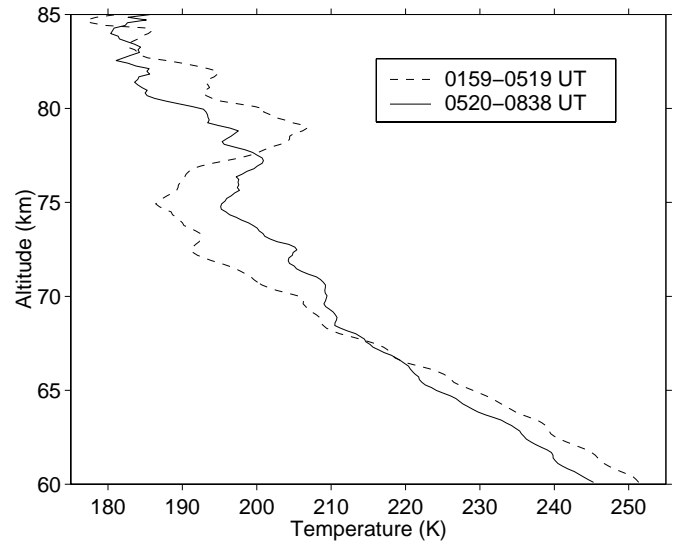

Figure 10. Comparison of mesospheric temperature profiles between the first and second halves of the observing period on June 1, 1996.
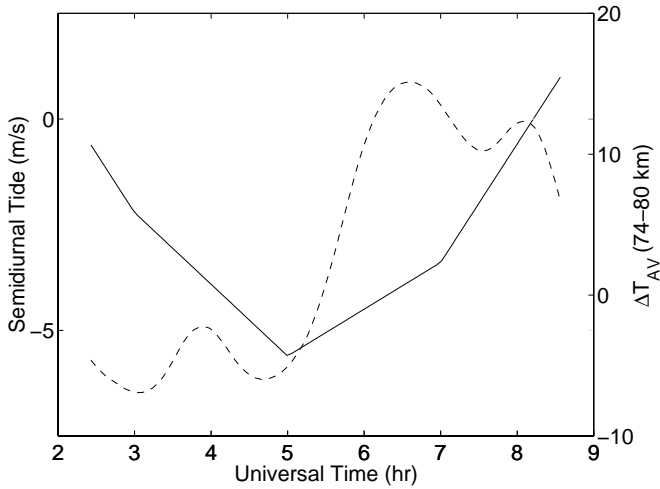

Figure 9. MF radar determinations of the semidiurnal tide compared to the temperature increase in the inversion region on July 31, 1998.

Figure 11. MF radar determinations of the diurnal plus the semidiurnal tide compared to the temperature increase in the inversion region on June 1, 1996.

pheric lapse rate in the first half of the measurement period. On this night both the diurnal and semidiurnal zonal tides are significant. Again, as the amplitude of the westward phase of the tide decreases, the strength of the inversion increases (Figure 11).

The combined effect of both the mean and tidal circulations on the June and July nights is such that the overall circulation during these periods is almost entirely eastward during the period of lidar measurements. This eastward bias in the mean wind would allow for considerable growth of westward travelling gravity waves, and, depending on the phase of the tide, slower moving eastward waves. Thus tidal-gravity wave interactions may determine the formation of the upper mesospheric inversions.

The dynamic nature of the temperature inversions can be masked by long-term averaging (i.e. over a
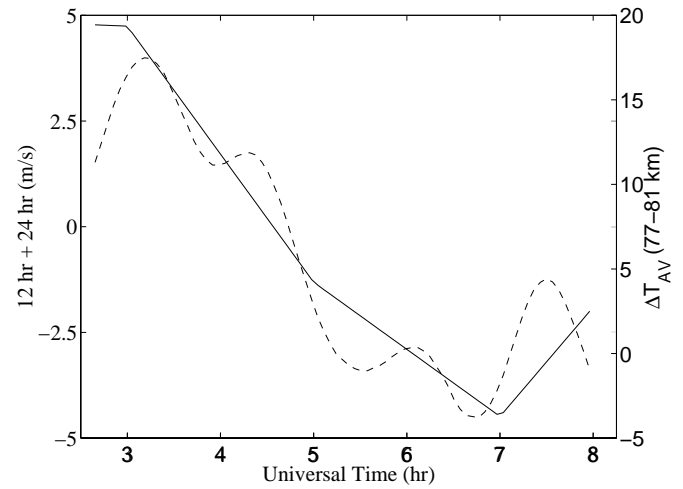
night), or possibly missed entirely by instruments which fail to sample the inversion during an "on" state (such as a spacecraft which only samples at a single local time). Though the inversion layers are dynamic and are always accompanied by extended regions of increased lapse rate below, they do no appear to be associated with significant changes in atmospheric stability (as indicated by lidar-derived lapse rates) or extreme kinetic energy densities (as determined from the lidar density perturbation measurements).

Knowledge of the differences (if any) in the lower atmospheric source spectrum of gravity waves on these nights would be helpful in determining whether our speculations are correct. Though our interpretation of the measurements seems reasonable, further progress in understanding the physical processes responsible for these measurements will require the aid of a tidal-grav-

ity wave interaction model (e.g. Liu and Hagan (17)). We plan such collaborative studies in the near future.

V. MEASUREMENTS OF GRAVITY WAVES

The importance of gravity waves in maintaining the structure and large-scale circulation of the middle atmosphere has driven many theoretical and observational studies on their effects. These investigations have revealed that the long-term spectral characteristics of these wave motions are remarkably uniform in frequency and wavenumber throughout the atmosphere, in spite of widely disparate locations and altitudes. However, our understanding of the processes that govern the formation and evolution of these spectra is still quite rudimentary as there are very few observations of the gravity wave spectrum at high spatial-temporal resolution.

Measurements by the PCL have shown that the environment the gravity waves propagate in is analogous to a lake full of white-cap waves. Evidence for these white-caps is shown by PCL measurements of superadiabatic layers in the upper stratosphere and mesosphere (18). Layering on the night of October 12, 1995 is shown in Figure 12. On this night substantial regions of stability exist in the upper stratosphere below 40 km, with the number of unstable regions increasing above this altitude.

Sica and Thorsley (19) studied four groups of measurements obtained in the spring, summer and fall. They showed that the "intensity" of the white caps is highly variable from month to month. They also presented some statistics of the layering (Figure 13). These results show the superadiabatic regions are extremely localized in time and space, while the regions of stability are extended in space and time. The disturbances caused by the gravity waves are consistent with the intermittency of the wave spectrum.

An example of this intermittency is shown in Figure 14 for vertical wavenumber spectra measured on the night of August 30, 1994. These spectra have been calculated using the covariance method of autoregressive
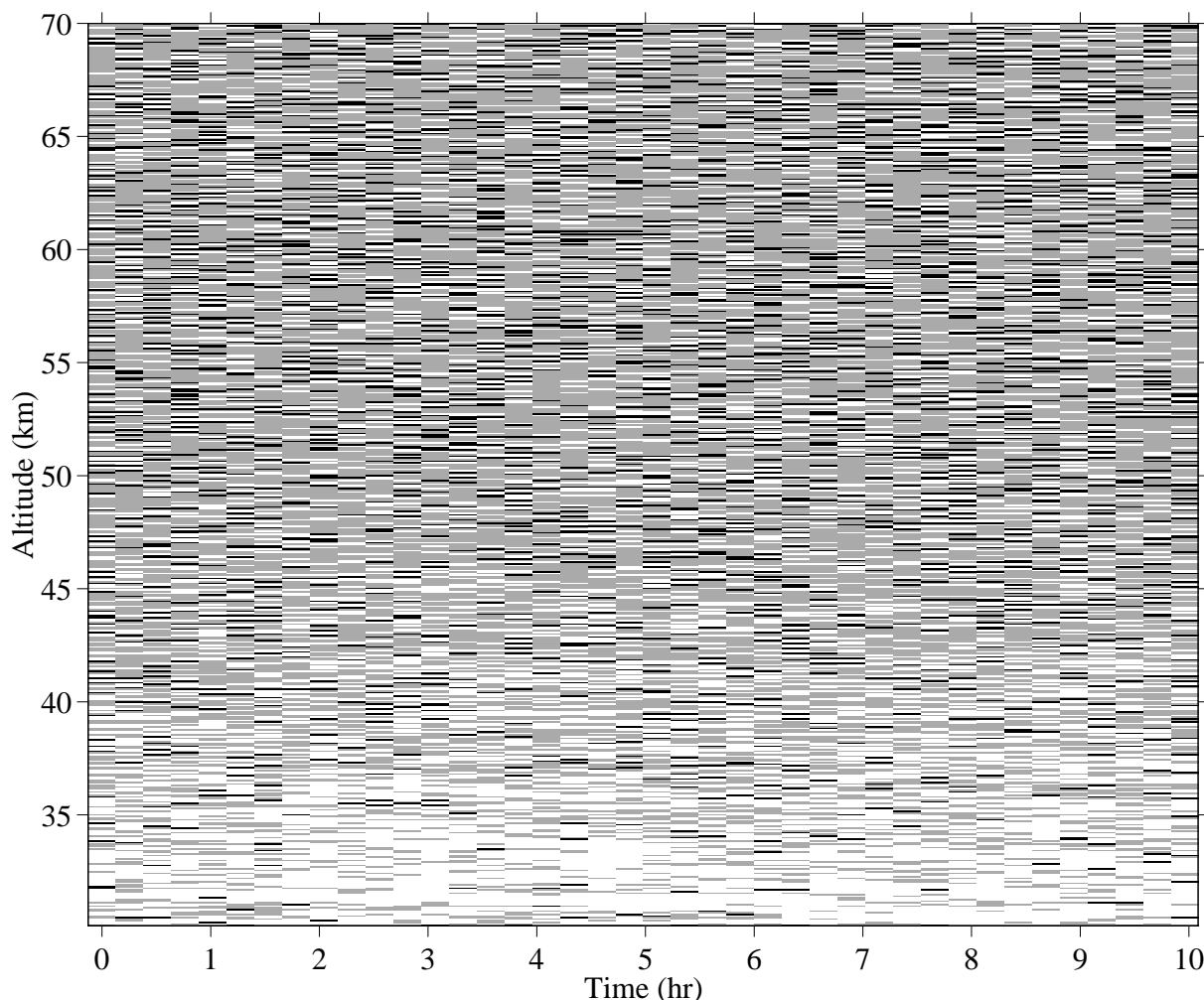

Figure 12. Determinations of superadiabatic layers on October 12, 1995. Superadiabatic regions are black, regions of absolute stability are white and indeterminate regions are gray. "0 hr" corresponds to 2024 EDT.
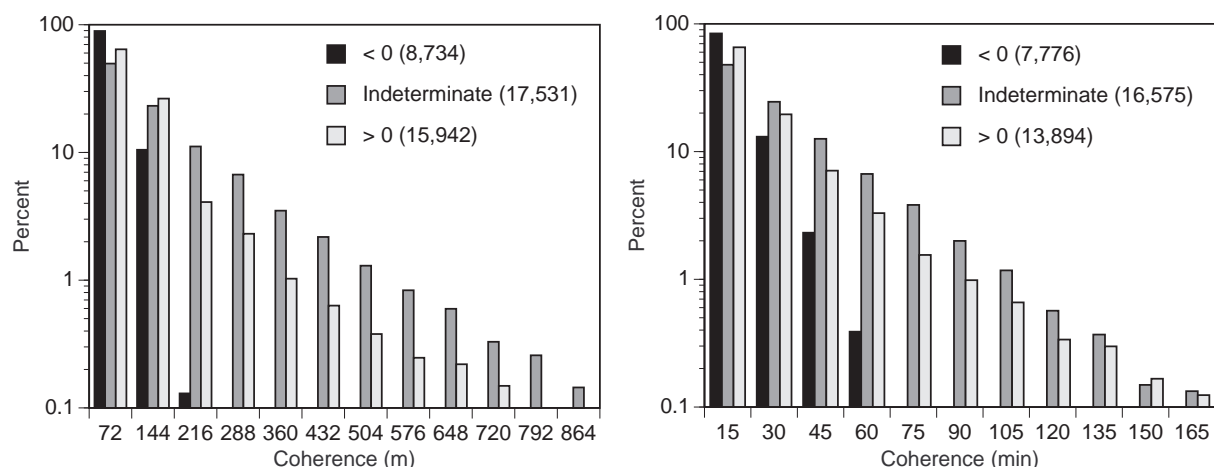
Figure 13. Spatial (left) and temporal (right) coherence of atmospheric layers for an ensemble of 9 nights measurements. The numbers in brackets are the number of measurements in each distribution.

power spectral density (PSD) estimation, details of which are given by Sica and Russell (20). Isolated coherent features are quite apparent in these spectra, especially at lower wavenumbers. The peak magnitude of individual spectra are also quite variable, with a low of 25 J/m^3 at 0830 UT to a maximum of 858 J/m^3 at approximately 0420 UT. It should be emphasized that these variations are geophysical and not signal-to-noise

or model order artifacts. The photon noise floors are essentially constant over the measurement period, while the features persist over a wide variety of model orders.

The intermittency of these features also precludes any kind of definitive slope determination on shorter time scales, as the intermittent features ride on a background that has a nominal slope of -2 to -3. If sufficient averaging is performed, a smooth vertical wavenumber
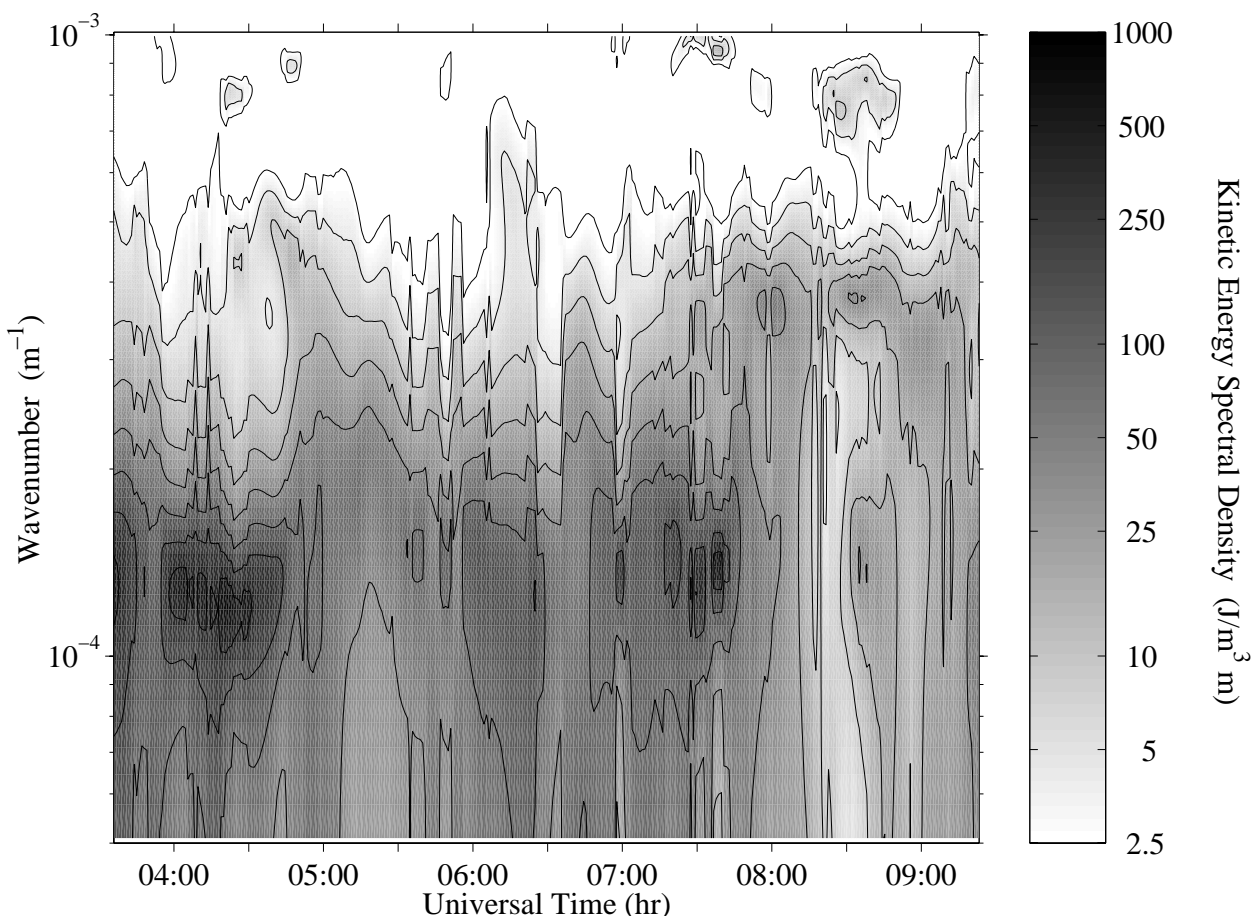

Figure 14. Upper stratospheric kinetic energy power spectral density on the night of August 30, 1994. The photon noise floors have been removed from the individual spectral estimates, which are separated by 1 min in time.

spectrum with the expected -3 slope will be obtained, providing a check on the signal-to-noise ratios of the measurements.

This averaging of high resolution spectra with quasi-monochromatic features into an apparently smooth continuous spectrum suggests that the gravity wave spectrum may actually be composed of a mixture of quasi-monochromatic waves and a broad spectrum. Sica and Russell (22) use Prony's method (21) to fit exponentially damped sinusoids to the upper strato-spheric density perturbation data series. The resulting fits are typically dominated by 3 or 4 quasi-monochro-matic features at lower wavenumbers. Sica and Russell also show that classical statistical PSD estimators, like the periodogram and correlogram, tend to blend these features into a continuous power law due to their inher-ently poor spectral resolution. Parametric PSD estima-tors are a much better choice for higher resolution studies because they are much more adept at isolating the individual waves in the spectrum.

This dominance of only a few quasi-monochromatic features in upper stratospheric vertical wavenumber spectra may also help explain why Lindzen-type gravity wave parametrizations appear to work in general circu-lation models. For instance, Hamilton (23) has shown that the climatology of the GDFL SKYHI general circu-lation model at high resolution with no explicit gravity wave parameterization scheme (e.g. the model generates its own gravity waves which can then interact with the mean wind) is in general agreement with a lower resolu-tion SKYHI calculation that uses a simple Lindzen-type parameterization scheme.

Prony's method also allows one to estimate the energy dissipated by individual gravity waves through the relation

$$\varepsilon = \frac{1}{2}(\alpha v_g U_x^2),\qquad(2)$$

where ε is the energy dissipated by the wave, α is the growth rate of the wave, v_g is the group velocity of the wave packet, and U_x is the horizontal wind perturbation induced by the gravity wave (24). The group velocity and the horizontal wind perturbation can be inferred from the wave's vertical phase velocity and amplitude respectively. Sica (25) calculated energy dissipation for an individual wave (using Equation (2)) as well as by integrating moments of the temporal spectrum. The
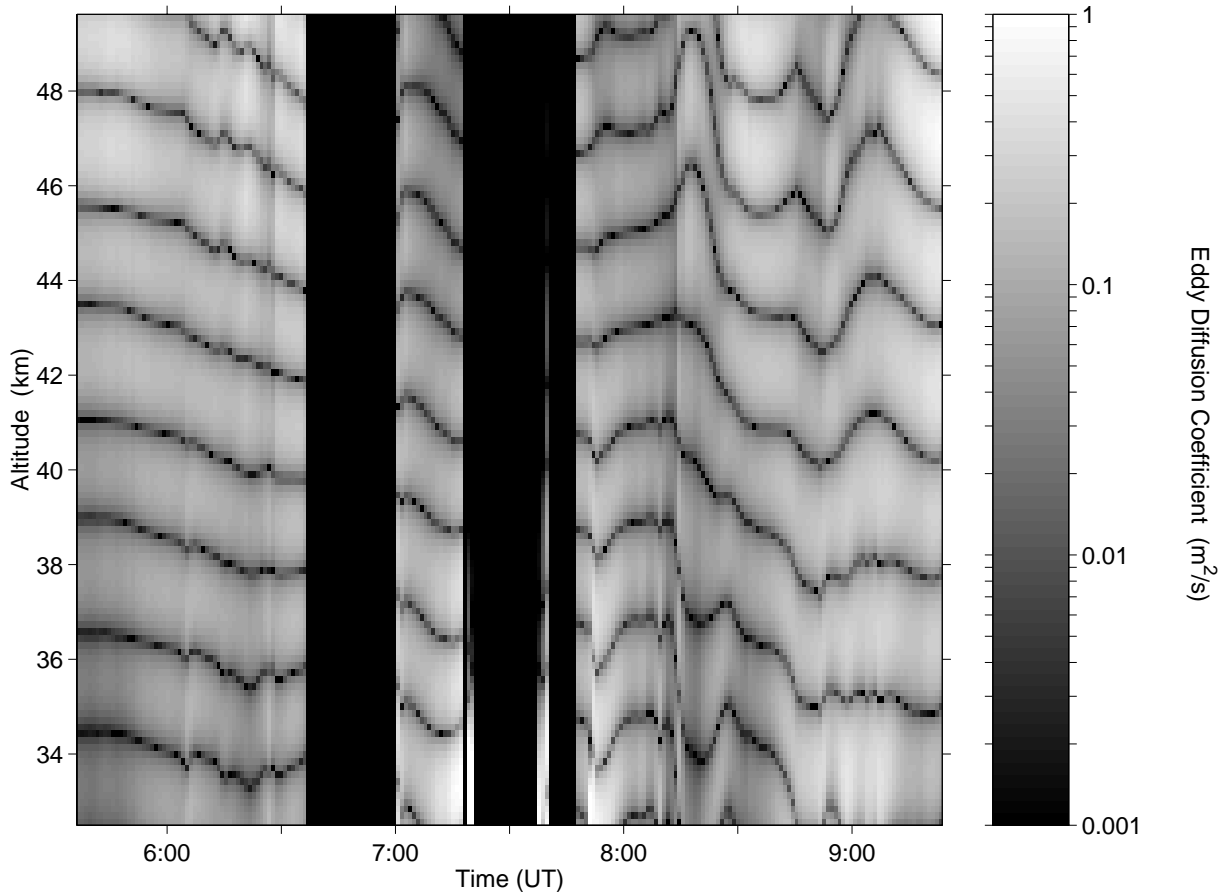

Figure 15. The eddy diffusion coefficient for a low wavenumber wave on the night of August 30, 1994. Note the broad band of high dissipation relative to the minima.

resulting energy dissipations were similar, on the order of 1 to 10 mW/kg in the upper stratosphere. The resulting energy dissipations were then used to estimate an eddy diffusion coefficient.

The eddy diffusion coefficient, D, can be inferred from

$$D = \beta \frac{\varepsilon}{N^2}, \qquad (3)$$

where N^2 is the angular buoyancy frequency, and β is a constant. Most studies assume that β is independent of time, with values in the range of 0.2 to 1.0 being most common. However, it has been shown by McIntyre (26) that β is actually a function of the vertical wavenumber spectrum's saturation. The parametric models employed in these studies allow the saturation-dependent β to be estimated as a function of time, with the somewhat surprising result that β is 5 to 10 times smaller than typically assumed. It also suggests that the variations in the vertical wavenumber spectrum, and their associated effects on β, may be the largest source of uncertainty in the determination of the eddy diffusion coefficient.
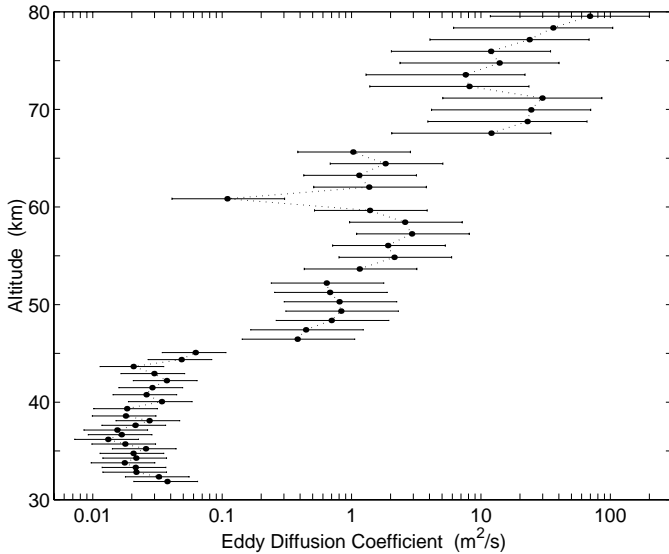
Figure 16. The eddy diffusion coefficient for the upper stratosphere and mesosphere on the night of August 30, 1994. The horizontal bars give a measure of the variability due to the value of β (as discussed in the text).

The eddy diffusion coefficient for a low wavenumber wave using the average value of the saturation dependent β is shown in Figure 15. The eddy diffusion is large over a broad region relative to the minima. The total eddy diffusion coefficient (i.e. using all waves out to 1 x 10^{-3} m^{-1}) is shown in Figure 16. This result is in reasonable agreement with previous determinations of the eddy diffusion coefficient (27) Though the gravity wave energy dissipation is large the vertical wavenum-

ber spectrum is sufficiently far from saturation that β is small, so the resulting eddy diffusion coefficient is consistent with previous results.
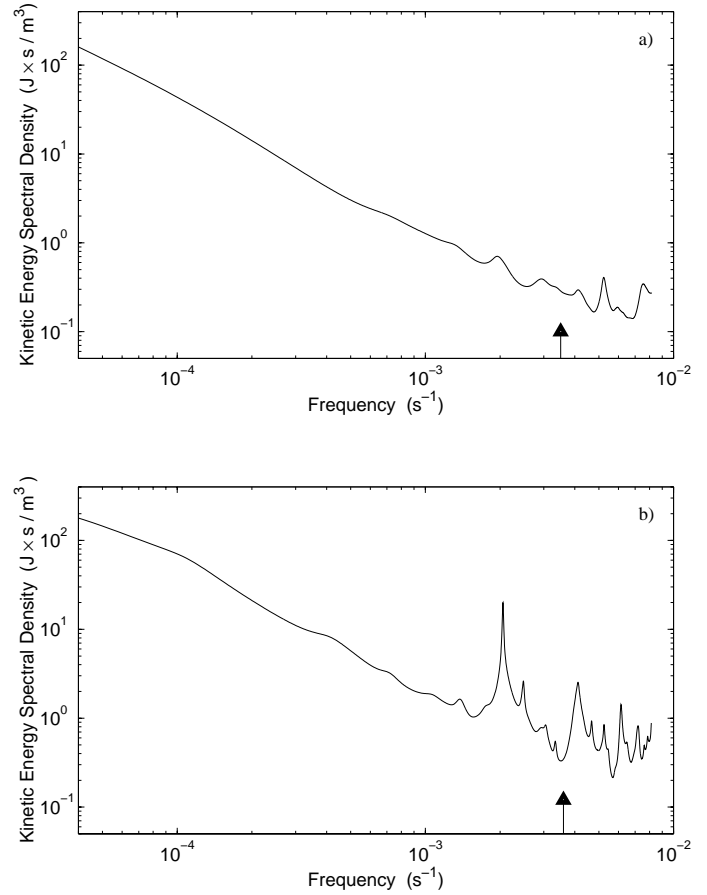
Figure 17. Mean temporal spectra in the upper stratosphere on the nights of (a) August 22, 1995 (32 to 37 km altitude) and (b) August 30, 1994 (32 to 38 km altitude). The arrows mark the mean measured buoyancy cutoff for the respective measurement periods.

Russell and Sica (28) have presented high resolution temporal gravity wave spectra in the stratosphere. The mean temporal spectrum for the night of August 22, 1995 (Figure 17a) is a classic example of a temporal gravity wave spectrum, e.g. the spectrum has a slope of -1.54 ± 0.01 over the frequency range 4.65×10^{-5} s^{-1} to $1.0\,0 \times 10^{-3}$ s^{-1}. This spectrum also shows minor Doppler-shifting effects past the measured buoyancy cutoff. The more structured temporal spectrum on August 30, 1994 has significant high frequency structure. The feature at 2.05×10^{-3} s^{-1} is striking, rising an octave (or more) above the background. The high frequency features are believed to be associated with parametric subharmonic instabilities, a class of nonlinear wave interactions. There is also a significant amount of power Doppler-shifted past the measured buoyancy frequency, with most of the Doppler shifting effects occurring in the 30 to 35km altitude region.

The presence of these higher frequency features in the temporal spectra suggests that wave activity in the stratosphere may be larger than that found in general circulation models. These features also suggest that significant amounts of energy may be dissipated in the middle upper stratosphere at certain times. This result has important implications in the determination of upper stratospheric eddy diffusion coefficients, as well as the interpretation of the wave spectrum obtained from general circulation models.

VI. TROPOSPHERIC AND LOWER STRATOSPHERIC WATER VAPOUR

Water vapour is perhaps the most important minor constituent, particularly in the troposphere. Water vapour absorbs radiation which helps drive the atmospheric circulations. Water vapour also modifies the radiative transfer of infrared absorption and can condense to form clouds. Improved measurements of tropospheric water vapour can lead to a better understanding of cloud formation, convective storm development, and the hydrological cycle.

Water vapour mixing ratios are usually conserved for most atmospheric processes (evaporation and condensation are the exceptions). Thus, it can used as a tracer of air parcels (29,30). When used as a tracer, water vapour measurements of sufficient temporal-spatial bandwidth can be used in studies of stratosphere-troposphere exchange.

Lower stratospheric water vapour also has important chemical considerations as a source for hydroxyl radicals, which are important in the cleansing the atmosphere of many anthropogenic compounds, including chlorine and nitrogen species. Water vapour also has an important role in the chemistry of stratospheric ozone.

Despite its importance, knowledge of the mean distribution of water vapour, its seasonal variability, and the processes that control it are limited. The Purple Crow Raman-scatter Lidar (PCRL) is now configured to obtain routine measurements of water vapour mixing ratio in the troposphere and lower stratosphere. Water vapour mixing ratios are obtained from the returned photocount profiles. After appropriate processing (for background signal, count nonlinearity, etc.), the photocount profiles can be used to determine the water vapour volume mixing ratio, $W(z)$, since

$$W(z) = R_{N_2} \cdot \frac{[\varepsilon\sigma\tau(z)]_{N_2}}{[\varepsilon\sigma\tau(z)]_{H_2O}} \cdot \frac{N_{H_2O}(z)}{N_{N_2}(z)}. \qquad (4)$$

The ratio of the N_2 density to that of dry air, R_{N_2}, is assumed constant with altitude. The term $[\varepsilon\sigma\tau(z)]$ is the product of the photomultiplier quantum efficiency, the vibrational Raman scattering cross section, and the atmospheric transmission at the appropriate wavelengths for scattering from N_2 and water vapour, 607.3 nm and 660.3 nm respectively. These factors convert the ratio of the corrected photocounts, $N_{H_2O}(z)/N_{N_2}(z)$, into units of ppmv. Since the photocount profiles measured by the PCRL are collected simultaneously and then used to determine a ratio, system variations such as laser power fluctuations which affect both profiles in the same manner, cancel each other out (see Section II.2).
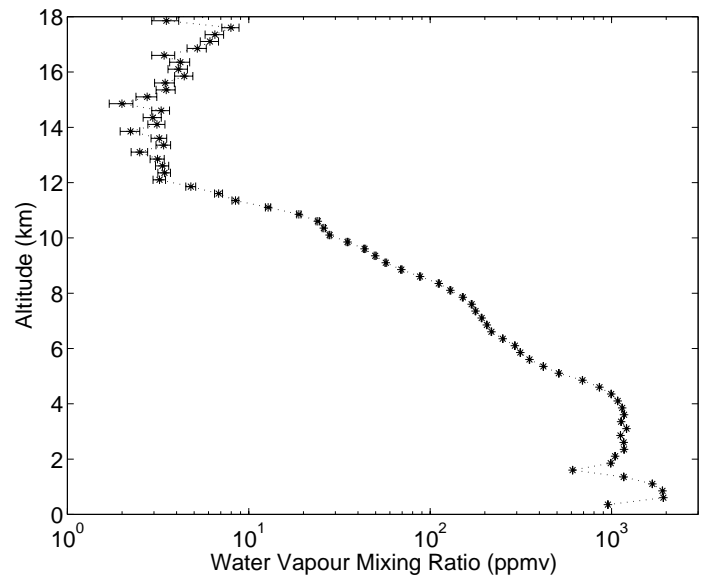

Figure 18. Typical nightly averaged water vapour profile for approximately 7 hours of integration on May 10, 1999.

The Purple Crow Raman-scatter Lidar has recently begun a program to measure water vapour in the lower stratosphere (31,32). Figure 18 shows the average mixing ratio profile on May 10, 1999 UT. This profile, typical of most nights, has a temporal resolution of about 7 hours and a spatial resolution of 250 m. It has a characteristic sharp decrease in water vapour mixing ratios near the tropopause and an average mixing ratio of about 4 ppmv above 12 km. Above 16 km the profile begins to vary due to the larger errors in the measurements at these altitudes. In the troposphere, the profile shows much larger values for the mixing ratios, especially near the surface.

Mean nightly profiles are particularly important in the lower stratosphere. Although satellites (such as the Stratospheric Aerosol and Gas Experiment II (SAGE II)) and aircraft measurements (such as NASA's ER-2 stratospheric aircraft) have begun to measure and study upper tropospheric and stratospheric water vapour, no

long-term databases of water vapour measurements in these regions exist. The PCRL is the only mid-latitude ground-based system able to make routine water vapour measurements in the lower stratosphere at middle latitudes.

The mean value of the mixing ratio on May 10, 1999 is between 3.5 to 4 ppmv between 12 and 15 km, with statistical errors of about 2% at 10 km, 12% at 15 km and 17% at 18 km (Figure 19). The mixing ratios values are consistent with measurements obtained by balloon-borne frost-point hygrometers from Boulder, Colorado between 1981 and 1994 by Oltmans and Hofmann (33). Another similarity to the Oltmans and Hofmann measurements is that the mixing ratio values drop sharply just above the troposphere. This decrease is due to the isothermal layer at the tropopause which prevents significant vertical mixing of water vapour into the stratosphere.
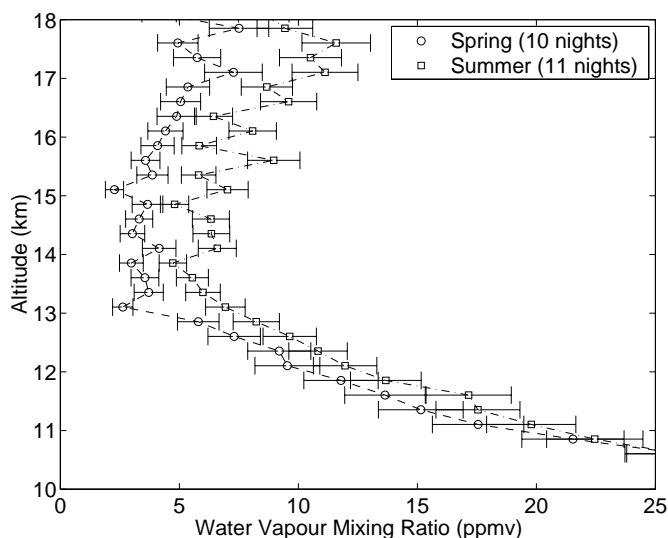

Figure 20. Water vapour measurements at 4 minutes temporal resolution and 250 m vertical resolution on May 10, 1999.

drops off from a value near 2400 ppmv to values below 1600 ppmv. This decrease is attributed to the capping inversion of the convective boundary layer (29). A large, moist region extending from 3 to 5 km appears above the Delaware Observatory. This type of feature is described by Melfi et al. (29) and is due to the passage of a frontal system. Meteorological maps from this period are consistent with this interpretation as the edge of a cold front passed near the observatory during this time. Integrated relative humidity (approximately the average relative humidity from 850 to 500 mb) determined from meteorological analysis during this period show variations similar to the PCRL mixing ratios measurements. Both the analysis and the PCRL observe a similar increase in the integrated relative humidity between 0000 and 1200 UT.

It has been suggested by the Stratospheric Processes And their Role in Climate (SPARC) project that studies of stratosphere-troposphere exchange require measurement errors to be about 5 to 10%, a figure of merit satisfied by the PCRL nightly profiles. We will use these measurements both to characterize the dynamics of stratospheric "middleworld" air as well as to characterize the intrusion of stratospheric air into the troposphere during exchange events.

Figure 19. Average of PCL water vapour measurements for the late spring compared to summer, 1999 in the lower stratosphere. The horizontal bars show the total of the statistical error and geophysical variation.

Oltmans and Hofmann have also shown that a seasonal variation exists in stratospheric water vapour. Spring mixing ratios are lower than summer mixing ratios just above the tropopause, but converge to approximately the same values at higher altitudes. The PCL measurements in the late spring and summer of 1999 show a similar variation (Figure 19).

The PCRL averages only span two and a half months (versus the 14 years of Oltmans and Hofmann's measurements). A larger database comprising several years is necessary to quantify any seasonal differences.

Figure 20 shows the May 10, 1999 measurements at higher spatial-temporal resolution in the troposphere. The water vapour mixing ratio from the surface to about 1.5 km is nearly constant. At 1.5 km the mixing ratio
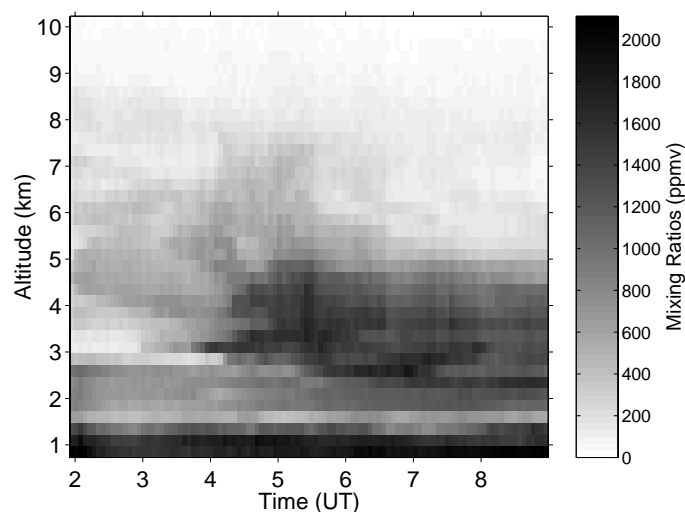
VII. N_2 AND O_2 DENSITY PROFILES

At altitudes in the upper mesosphere and lower thermosphere, temperatures can be determined from both the Rayleigh and sodium resonance fluorescence lidar measurements. PCL measurements of these two sets of temperatures are compared by Argall et al. (1) and found to significantly disagree at times. The temperatures derived from the Rayleigh-scatter technique

assume that the atmospheric constituent mixing ratio and cross section are constant with altitude and equal to their sea level values (3). However, the Na lidar temperature is a direct measure of the kinetic temperature of the atmosphere (34-36). The disagreement found in Argall et al. suggests that the mixing ratio of the major atmospheric constituents is not always equal to its sea level value in the upper mesosphere and lower thermosphere. Neutral composition measurements made by rocket borne mass spectrometers have also observed differences from the sea level values in this altitude region (37-42).
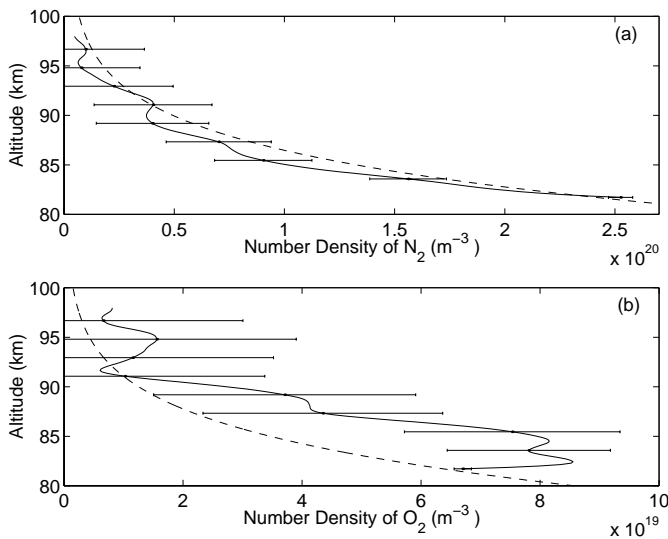

Figure 21. The solid black curves are our measured densities of N_2 and O_2 averaged over the time interval 0231 to 0835 UT on the night of May 24, 1998. The error bars indicate the random uncertainties in these measurements. The dashed curves are the densities predicted by the MSIS-E-90 model.

Assuming that the temperatures derived from the sodium resonance fluorescence backscatter are the true atmospheric temperature, it was shown by Mwangi et al. (34) that the densities of N_2 and O_2 can be derived from the Na temperature profiles and the Rayleigh backscatter measurements. The technique involves solving a system of ordinary differential equations derived from the lidar equation, the Ideal Gas Law, and hydrostatic equilibrium. An example of the composition retrieval using PCL measurements is shown in Figure 21. These results are consistent both with the composition measurements referenced above and empirical atmospheric models. Measurements of these densities will be important for understanding the coupling between the dynamics and the chemistry in the upper mesosphere and lower thermosphere, as well as improving the retrieval of temperatures from Rayleigh-scatter systems in the lower thermosphere.

VIII. FUTURE DIRECTIONS

We have two major upgrades planned for our measurements program. The first is the addition of the necessary equipment to allow our sodium laser system to measure winds in a manner similar to Bills el al. (44). With the large power-aperture product of our system we anticipate being able to measure vertical winds and heat fluxes due to gravity waves. This upgrade is in progress at the present time.

The second improvement is to our composition measurements in the upper troposphere and lower stratosphere. In addition to N_2 and water vapour we plan on adding detection capability for CH_4 and CO_2. Both CH_4 and CO_2 are important Greenhouse gases. However, because of the stringent measurement signal-to-noise requirements, no routine measurements of these important gases are currently being made by ground-based systems.

REFERENCES

1. Argall, P.S., Sica, R. J., Vassiliev, O. & Mwangi, M. M. 2000. Appl. Opt. In press.

2. Sica, R. J., Sargoytchev, S., Argall, P. S. Borra, E. F. Girard, L. Sparrow, C. T. & Flatt, S. 1995. Appl. Opt. 34, 6925.

3. Chanin, M. L. & Hauchecorne, A. 1980. Geophys. Res. Lett., 7, 565.

4. Shibata, T., Kobuchi, M, & Maeda, M. 1986. Appl. Opt., 31, 2095.

5. Sica, R. J., Zylawy, Z. A. & Argall, P. S. 2000. App. Opt. Submitted.

6. Fleming S. S., Chandra, M., Schoeberl, M. & Barnett, J. 1988. NASA Technical Memorandum, #NASA TM-100697.

7. Senft D. C., Papen, G. C., Gardner, C. S., Yu, J. R.,. Krueger, D. A. & She, C. Y. 1994. Geophys. Res. Lett., 21, 821.

8. Schmidlin, F. J. 1975. Geophys. Res. Lett., 3, 173.

9. Hauchecorne, A., Chanin, M. L. & Wilson, R. 1987. Geophys. Res. Lett., 14, 933.

10. Leblanc, T. & Hauchecorne, A. J. 1997. J. Geophys. Res. 102, 19,471.

11. Whiteway, J. A., Carswell, A. I. & Ward, W. E. 1995. Geophys. Res. Lett., 22, 1201.

12. Dao, P. D., Farley, R., Tao, X. & Gardner, C. S. 1995. Geophys. Res. Lett., 20, 2825.

13. States, R. J. & Gardner, C. S. 1998. Geophys. Res. Lett., 25, 1483.

14. Meriwether, J. W., Gao, X., Wickwar, V. B., Wilkerson, T. Beissner, K. Collins, S. & Hagan, M. E. 1998. Geophys. Res. Lett., 25, 1479.

15. Sica, R. J., Thayaparan, T., Argall, P. S. Russell, A. T. & Hocking, W. K. 2000. J. Geophys. Res., submitted.

16. Thayaparan, T., Hocking, W. K. & MacDougall, J. 1995. Radio Sci. 30, 1293.

17. Liu, Han-Li & Hagan, M. 1998. Geophys. Res. Lett., 25, 2941.

18. Sica, R. J. & Thorsley, M. D. 1996. Geophys. Res. Lett., 23, 2797.

19. Sica, R. J. & Thorsley, M. D. 1997. In: Hamilton, K. (Editor), Gravity Wave Processes. Their Parameterization in Global Climate Models, page 27, Springer-Verlag, Berlin.

20. Sica, R. J. & Russell, A. T. 1999. J. Atmos. Sci., 56, 1308.

21. Marple, S. L. 1987. Digital Spectral Analysis. Chapter 11, Prentice Hall, Englewood Cliffs, NJ.

22. Sica, R. J. & Russell, A. T. 1999. Geophys. Res. Lett. 26, 3617.

23. Hamilton, K. 1997. In: Hamilton, K. (Editor), Gravity Wave Processes. Their Parameterization in Global Climate Models, page 337, Springer-Verlag, Berlin.

24. Hines, C. O. 1965. J. Geophys. Res. 70, 177.

25. Sica, R. J. 1999. J. Atmos. Sci., 56, 1330.

26. McIntyre, M. E 1989. J. Geophys. Res., 89, 14617.

27. Hocking, W. K. 1991. J. Geomagn. Geoelectr. 43 (Suppl.), 621.

28. Russell, A. T. & Sica, R. J. 2000. J. Geophys. Res. Submitted.

29. Melfi, S. H., Whiteman, D. N. & Ferrare, R. A. 1989. J. App. Meteor. 28, PAGE.

30. Whiteman, D. N., Ferrare, R. A. & Melfi, S. H. 1992. App. Opt. 31, PAGE.

31. Bryant, C. R. 1999. M. Sc. Thesis, The University of Western Ontario.

32. Bryant, C. R., Argall, P. S. & Sica, R. J. 2000. App. Opt. Submitted.

33. Oltmans, S. J. & Hofmann, D. J. 1995. Nature. 374, 146.

34. Gibson, A., Thomas, L. & Bhattachacharyya, S. 1979. Nature, 281, 131.

35. Fricke, K. H., & von Zahn, U. 1985. J. Atmos. Terr. Phys., 47, 49.

36. She, C. Y., Yu, J.R. Latifi, H & Bills, R. E. 1992. Appl. Opt., 31, 2095.

37. Philbrick, C. R., Faucher, G. A. & Trzcinsky, E. 1973. Space Research, 13, 255.

38. Philbrick, C. R., Golomb, D., Zimmerman, S. P., Keneshea, T. J., MacLeod, M., Good, R. E., Dandekar, B. S. & Reinisch, B. W. 1974. Space Research, 14, 89.

39. Philbrick, C. R, Faucher, G. & Bench, P. 1978. Space Research, 18, 139.

40. Trinks, H., Offermann, D., von Zahn, U. & Steinhauer, C. 1978. J. Geophys. Res., 83, 2169.

41. Krankowsky, D., Arnold, F., Friedrich, V. H. & Offermann, D. 1979. J. Atmos. Terr. Phys., 41, 1085.

42. Offermann D., Friedrich, V., Ross, P. & von. Zahn, U. 1981. Planet Space Sci., 29, 747.

43. Mwangi, M. M., Sica, R. J. & Argall, P. S. 2000. J. Geophys. Res. Submitted.

44. Bills, R. E., Gardner, C. S. & She, C. Y. 1991. Opt. Eng., 30, 13.